Highly dispersed Pt–MnO$_x$ nanoclusters for the promoted activity of mesoporous Pt–MnO$_x$–Al$_2$O$_3$ in dehydrogenation of perhydro-benzyltoluene

Yeongin Jo [a],[1], Donghyeon Kim [a],[1], Tae Wan Kim [a], Doohoo Yoon [a], Young-Woong Suh [a],[b],[*]

[a] *Department of Chemical Engineering, Hanyang University, Seoul 04763, Republic of Korea*
[b] *Research Institute of Industrial Science, Hanyang University, Seoul 04763, Republic of Korea*

ARTICLE INFO

ABSTRACT

Pt single atom is vulnerable to sintering under endothermic reaction conditions and sometimes shows low activity in the conversion of bulky molecules, e.g., dehydrogenation of perhydro-benzyltoluene (H$_{12}$-BT) for the state-of-the-art liquid organic hydrogen carrier system. Such weakness has been tackled using various approaches including Pt nanoclustering with metal oxide(s). We herein describe the excellence of mesoporous Pt–MnO$_x$–Al$_2$O$_3$ (mPtMnA) in H$_{12}$-BT dehydrogenation, where solvent-deficient precipitation (SDP) is employed for catalyst preparation. When prepared at the Mn/Pt molar ratio of 0.33 and the ramp of 10 °C min^{-1} in H$_2$ reduction, the catalyst (named mPt0.33MnA_r10) affords the best efficiency of 94 % H$_2$ yield. This results from highly dispersed Pt–MnO$_x$ nanoclusters generated by the surface diffusion of Pt atoms to oxophilic Mn oxides distributed homogeneously on the surface of support. Consequently, this study demonstrates that the SDP method favors Pt nanoclustering with MnO$_x$, which will greatly impact on dehydrogenation catalysis.

1. Introduction

In a number of dehydrogenation reactions, supported Pt catalysts show excellent performance in the cleavage of C–H bond and can sufficiently lower the reaction temperature with byproducts being little formed [1,2]. To secure high Pt dispersion and thereby increase atomic utilization efficiency, γ-Al$_2$O$_3$ has been used as the most popular support. However, when conventional impregnation is used for Pt/Al$_2$O$_3$ system, Pt species of three forms, such as single atoms (SAs), nanoclusters (NCs), and nanoparticles (NPs), are generally produced on the surface of Al$_2$O$_3$ even if Pt loading is merely 1 wt% [3]. In most literature, SAs refers to a single atom or isolated atom as the name suggests, and NCs and NPs are divided on the basis of particle diameter of 2 nm (NCs smaller than 2 nm and NPs larger than 2 nm). As another classification, NCs are those that do not form crystal facets and are only agglomerated, while particles with well-developed crystal facets are categorized into NPs. In Pt-catalyzed dehydrogenation reactions, the active Pt species depends on the size of the reactant [4–8]; the representative molecules are propane and methylcyclohexane (MCH). In propane dehydrogenation, Pt SAs were reported to be excellent in

turnover frequency and propylene selectivity compared to Pt NCs and NPs [4]. However, the dehydrogenation of MCH, which is larger than propane, was favorable over Pt NCs with a size of approximately 1 nm [8]. Therefore, it is challenging to find and form the active Pt species that would be optimal for the molecular size of dehydrogenation reactant.

Recently, we developed mesoporous Pt–Al$_2$O$_3$ catalysts (mPtA) prepared by solvent-deficient precipitation (SDP) for the dehydrogenation of perhydro-benzyltoluene (H$_{12}$-BT) [9], which is the state-of-the-art liquid organic hydrogen carrier (LOHC) [10]. The LOHC concept is based on catalytic hydrogenation and dehydrogenation of liquid-phase organic media for H$_2$ storage and transportation. The widely-recognized bottleneck in LOHC systems is the dehydrogenation reaction that should work at high temperatures and employ expensive noble metal (e.g., Pt and Pd) catalysts. When the Pt content was 1 wt% in mPtA catalysts, the catalytic performance was poor because the catalyst mainly possessed Pt SAs that generally lose a part of metallic properties leading to the efficient adsorption of reactants [11]. Interestingly, the mPtA catalyst of 3 wt% Pt exhibited the best activity owing to the formation of Pt NCs along with Pt SAs. In addition, we attempted to

---

aggregate Pt SAs to NCs via tuning parameters of temperature and time in oxidative calcination. This approach offered limited advantages for the dehydrogenation of H_{12}-BT because of difficulty in achieving uniform distribution of Pt species.

Thus, we searched for another approach to combine Pt SAs with other metals or metal oxides for creating ensembles with high activity. Among many elements, Mn oxides (MnO_x), which themselves are hardly active in dehydrogenation reactions, are found to be frequently used for boosting the activity of Pt catalysts [12]. The promotion effects of MnO_x are summarized in two aspects: electron transfer and blocking of Pt defect sites. The electron transfer from Pt to MnO_x can reduce the electron density of Pt and thereby induce the charge of Pt atoms partially positive, which is beneficial for the activation of propane with the desorption of propylene [13]. On the other hand, MnO_x can preferentially bind to Pt defect sites (i.e., edge and corner sites), suppressing side reactions taking place in MCH dehydrogenation and improving the catalyst stability by the reduced adsorption of the dehydrogenation product [14].

To successfully derive these positive effects of Pt–MnO_x interaction, the intimate contact of the two components is desired. In particular, this is unconditionally required for low-content Pt catalysts in which Pt species (mostly, Pt SAs) and MnO_x are well dispersed over a support. In terms of controlling the interfacial contact between two components, a variety of synthetic approaches have been proposed so far, such as amount of additive [15], addition sequence of two components [16,17], and thermal treatment after catalyst synthesis [18,19]. Gan et al. recently reported that the interface of PtM_3 (M = Fe, Co, and Ni) catalysts could be tuned by changing the temperature in a reductive process [19]. This phenomenon was based on the difference in particle mobility under H_2 atmosphere, depending on the surface composition. Moreover, hydrogen selectively adsorbed to Pt species during H_2 reduction can lead to the increased surface mobility and the promoted aggregation of Pt SAs to NCs [20]. This surface mobility is based on the calculation result that the aggregation from Pt_1O_4 (Pt SAs) to Pt_{13} NCs is thermodynamically more stable due to enthalpic compensation.

Referring to these reports, we designed to produce highly dispersed Pt–MnO_x NCs in a mesoporous Pt–MnO_x–Al_2O_3 catalyst (nominal Pt loading: 1 wt%) prepared by the SDP method. First, we optimized the synthesis variables such as the addition sequence and content of Mn species, in order to find the catalyst showing the high activity in the dehydrogenation of H_{12}-BT. Here it should be noted that the employed Mn/Pt molar ratios were selected on the basis of the previous reported Mn/Pt ratios (~10/1) and intermetallic PtMn catalysts (1/3 to 3/1). Meanwhile, the synthesized catalysts along with those prepared by conventional impregnation were characterized to identify Pt species as well as Pt–MnO_x interaction. Then, we changed a ramp rate (2, 5, and 10 °C min^{-1}) at a step of H_2 reduction in preparing the selected catalyst and then examined its effect on the catalytic activity and properties. At this point, the best dehydrogenation performance was achieved over the catalyst with highly dispersed Pt–MnO_x NCs prepared by the ramp of 10 °C min^{-1}, which was not confirmed in the conventional Pt–MnO_x/Al_2O_3 catalyst. Furthermore, the formation of such NCs through fast H_2 reduction were investigated by performing iterative H_2 reduction and their stability was also verified through repeated reaction runs. Finally, various SDP-derived samples were characterized to understand the fundamental cause for the formation of highly dispersed Pt–MnO_x NCs. From a series of catalyst synthesis and characterization, we believe that the solvent-deficient environment generated by the SDP method greatly influences the species of Pt, Mn, and Al, as well as surface mobility of Pt species and interaction between Pt and MnO_x.

2. Experimental

2.1. Preparation of supported Pt catalysts

The SDP method was used for the preparation of mesoporous

Pt–MnO_x–Al_2O_3 catalysts with the Pt loading of 1 wt%. Typically, Pt $(NH_3)_4(NO_3)_2$ (Alfa Aesar), $Mn(NO_3)_2 \cdot 6 H_2O$ (Junsei Chemical), Al $(NO_3)_3 \cdot 9 H_2O$ (Junsei Chemical), and NH_4HCO_3 (Daejung Chemicals) without solvent were ground together by a pestle in a mortar for 20 min, where the molar ratio of total nitrates to ammonium bicarbonate was set at 1.0. The resulting gel-like samples were calcined at 600 °C for 5 h (ramp: 2 °C min^{-1}) and then reduced by H_2 at 500 °C for 3 h (ramp: 5 °C min^{-1}, otherwise specified). The prepared catalysts are denoted as $mPtxMnA$, where x represents the Mn/Pt molar ratio ranging from 0.18 to 3.14.

The SDP method was used to prepare mesoporous Al_2O_3 (mA) using only $Al(NO_3)_3 \cdot 9 H_2O$, mesoporous MnO_x–Al_2O_3 (m0.33MnA) using Mn $(NO_3)_2 \cdot 6 H_2O$ (the same amount used for the preparation of mPt0.33MnA) and $Al(NO_3)_3 \cdot 9 H_2O$, and mesoporous 1 wt% Pt–Al_2O_3 (mPtA) using $Pt(NH_3)_4(NO_3)_2$ and $Al(NO_3)_3 \cdot 9 H_2O$, where the molar ratio of total nitrates to ammonium bicarbonate was still set at 1.0. The first two samples (mA and m0.33MnA) were obtained by calcination at 600 °C for 5 h (ramp: 2 °C min^{-1}), while the latter mPtA catalyst was prepared by the same heat treatment as applied for mPtxMnA.

For comparison, Pt/γ-Al_2O_3 and Pt–Mn/γ-Al_2O_3 with the Pt loading of 1 wt% were prepared by incipient wetness impregnation (IWI) of Pt $(NH_3)_4(NO_3)_2$ and $Mn(NO_3)_2 \cdot 6 H_2O$ dissolved in distilled water onto γ-Al_2O_3 (STREM). After drying at 105 °C, the samples were subjected to the same calcination and H_2 reduction process as described above. These catalysts are named as Pt/gA and Pt–0.33Mn/gA. Also, the synthesized m0.33MnA and mPtA (calcined at 600 °C) was used as a support for loading of Pt or Mn, producing Pt/m0.33MnA and 0.33Mn/mPtA, respectively. The Mn/Pt molar ratio was fixed at 0.33 for Pt–0.33Mn/gA, Pt/m0.33MnA, and 0.33Mn/mPtA.

2.2. Activity tests for the dehydrogenation of H_{12}-BT

The reactant, perhydro benzyltoluene (H_{12}-BT), was prepared by the hydrogenation of purchased H_0-BT (Marlotherm® LH Charge No. 1717). Gas chromatography (GC) analysis confirmed that H_0-BT was fully hydrogenated to H_{12}-BT using Ru/MgO under the conditions of 0.08 mol% Ru/H_0-BT, 150 °C, 50 bar H_2, and 1200 rpm [21].

Dehydrogenation experiments were performed in a batch reactor of 120 cm^3 according to the reported procedure [9,22]. H_{12}-BT (7.72 mmol) was added dropwise to the catalyst pre-loaded at the reactor bottom, where the catalyst weight was determined to obtain the desired Pt/H_{12}-BT molar ratio. While purging with N_2 for 10 min, the reactor was heated to 250 °C using a jacket filled with a commercial heat-transfer fluid. The reaction was conducted for 220 min with the stirring of 200 rpm, where the volume of H_2 released was measured by a wet-gas meter. From the measured H_2 volume, the degree of dehydrogenation based on gas products ($DoDH_{gas}$) was calculated, as follows:

$DoDH_{gas}$ [mol%] = (H_2 volume recorded on a wet-gas meter [cm^3]) / (initial H_{12}-BT [mol] $\times$ 82 [$cm^3 mol^{-1} K^{-1}$] $\times$ 298.15 [K]) $\times$ 100 %.

After the experiment was finished, the reactor was cooled, and a portion of the product mixture (ca. 1.5 g) was diluted with acetone (10 mL) and then mixed with nonane as a calibration solvent (100 μL). The liquid sample was analyzed in an Agilent Technologies 7890 A GC equipped with a Restek Rxi®–17Sil column (30 m $\times$ 0.25 mm $\times$ 0.25 μm). The GC peak areas of H_{12}-BT (reactant), H_6-BT (intermediate), H_0-BT (product), and methyl fluorene (MF that is a byproduct formed by dehydrogenative cyclization of H_0-BT releasing another mole of H_2) were used to calculate H_{12}-BT conversion ($X_{H12\text{-}BT}$), H_x-BT selectivity (x = 0 for $S_{H0\text{-}BT}$ and x = 6 for $S_{H6\text{-}BT}$), MF selectivity (S_{MF}), and the degree of dehydrogenation based on liquid products ($DoDH_{liq}$), as follows:

$X_{H12\text{-}BT}$ = (initial H_{12}-BT [mol] – final H_{12}-BT [mol]) / (initial H_{12}-BT [mol]) $\times$ 100 %.

$S_{Hx\text{-}BT}$ (x = 0 and 6) = (final H_x-BT [mol]) / (final H_0-BT [mol] + final H_6-BT [mol] + final MF [mol]) $\times$ 100 %

S_{MF} = (final MF [mol]) / (final H_0-BT [mol] + final H_6-BT [mol] + final MF [mol]) × 100 %

$DoDH_{liq}$ = (final H_6-BT [mol] × 3 + final H_0-BT [mol] × 6 + final MF [mol] × 7) / (initial H_{12}-BT [mol] × 6) × 100 %

where the measured $DoDH_{gas}$ and calculated $DoDH_{liq}$ were within a margin of error (less than 2 %) although the former value is relatively more valid and reliable.

The tests for catalyst recyclability were performed using the regenerated catalyst that was acquired by collection of a solid catalyst after the reaction, washing with acetone, filtration, drying at 60 °C under a reduced pressure overnight, and H_2 reduction at the same condition as provided for catalyst preparation.

2.3. Catalyst characterization

The specific surface area, pore volume, and pore diameter of a sample were measured in a Micromeritics ASAP 2020 after vacuum degassing at 200 °C for 2 h. X-ray diffraction (XRD) analysis was performed with a Rigaku miniFlex600 diffractometer installed at the Hanyang LINC3.0 Center for Research Facilities(Seoul) using a Cu K_α radiation source operated at 40 kV and 15 mA, where XRD patterns were recorded in 2θ ranging from 10° to 80° at a scan rate of 10° min^{-1} and a step of 0.02°. The actual contents of Pt and Mn were measured by an inductively coupled plasma optical emission spectrometer (ICP-OES) using a Thermo Fisher Scientific iCAP 7400DUO instrument, where the samples dissolved in a mixture of HNO_3 and HCl (1:6, v/v) were pre-treated in a Milestone Ethos Easy Microwave digestion system before measurement. High angle annular dark field scanning transmission electron microscopy (HAADF-STEM) images were taken in a FEI Titan cubed G2 60–300 with an accelerating voltage of 300 kV. X-ray photoelectron spectroscopy (XPS) analysis was performed to determine the electron state and density of each element using a Thermo Scientific K-alpha+ spectrometer with a monochromatic Al $K\alpha$ source, where all spectra were collected with a step size of 0.1 eV and a pass energy of 50 eV, and corrected using the C 1 s binding energy of 284.5 eV. Notably, optimal fittings for Pt 4d and Mn 2p spectra were obtained based on the R^2 values of higher than 90 %, despite low signal-to-noise ratio due to the very small contents of Pt and Mn species.

H_2 temperature-programmed reduction (H_2-TPR) experiments were performed in a Micromeritics Autochem 2920, where a sample (ca. 200 mg) was heated at a ramp of 5 °C min^{-1} to 600 °C in a 10 % H_2/Ar flow of 50 cm^3 min^{-1} after oxidation at 500 °C in a 10 % O_2/He flow for 1 h and purge in an Ar flow at 50 °C for 30 min. CO-chemisorbed diffuse reflectance infrared Fourier transform (CO-DRIFT) spectra were obtained from a Bruker Tensor 27 spectrometer installed with a Harrick Praying Mantis high temperature chamber. Prior to analysis, a catalyst of 30 mg in a sample cup was pretreated at 300 °C in an Ar flow of 30

cm^3 min^{-1} for 1 h, followed by cooling to 50 °C. After a background spectrum was collected at 50 °C, the sample was exposed to a 1 % CO/He flow of 30 cm^3 min^{-1} until CO adsorption was saturated. Finally, CO-DRIFT spectra were taken while physisorbed CO molecules were removed in an Ar flow of 30 cm^3 min^{-1} for 15 min

3. Results and discussion

3.1. Catalytic activity and properties of the mPtMnA catalysts

The mPtMnA catalysts with different Mn/Pt molar ratios were tested in the dehydrogenation of H_{12}-BT at 0.3 mol% Pt/H_{12}-BT and 250 °C (Table S1). The time-dependent $DoDH_{gas}$ curves display that all mPtMnA catalysts were superior to mPtA (62.5 % $DoDH_{gas}$), except mPt3.14MnA containing excess Mn to possibly block Pt particles (Fig. 1a). In addition, as the Mn/Pt molar ratio increased, the rate of H_2 release was improved in the latter part of the reaction. For example, the activities of mPt0.18MnA and mPt0.62MnA were reversed after reaction time of 100 min at which the conversion, selectivity, and DoDH were nearly identical (Table S2). The results measured at 220 min revealed that mPt0.62MnA formed less H_6-BT and more H_0-BT than mPt0.18MnA, supporting that the dehydrogenation of H_6-BT to H_0-BT is faster in mPt0.62MnA. Therefore, the different rate of H_2 release with increasing the Mn/Pt molar ratio is associated with the lowered electron density of Pt species [22], which will be discussed later.

When the $DoDH_{gas}$ value measured at 220 min was plotted against the Mn/Pt molar ratio, a volcano-shaped trend was obtained at the maximum with mPt0.33MnA showing 83.3 % $DoDH_{gas}$ (Fig. 1b). The identical trend was observed in the plot of $DoDH_{liq}$ against the Mn/Pt molar ratio (Fig. 1b). Furthermore, the first-order rate constant (k) was calculated from the slope in the plot of $\ln(1 - X_{H12-BT})$ against the reaction time ranging from 0 to 10 min during which the conversion of H_{12}-BT was usually less than 10 % (Fig. S1). The k value also showed the volcano-shaped curve with respect to the Mn/Pt molar ratio (Fig. 1b). From the fact that the activity of m0.33MnA was very poor, the above results manifest that Mn species acts as a promoter to boost the dehydrogenation performance of active Pt species in mPtA.

To ascertain the promoted activity of mPtMnA catalysts, the IWI method was additionally used for Pt loading, where the Mn/Pt molar ratio was fixed at 0.33. When γ-Al_2O_3 (gA) was used as a support, the co-impregnated Pt–0.33Mn/gA (78.8 % $DoDH_{gas}$) was a little more active than Pt/gA (75.1 % $DoDH_{gas}$) in the dehydrogenation of H_{12}-BT, which was caused by the similar X_{H12-BT} and higher S_{H0-BT} between the two catalysts (entries 1 and 2 in Table 1). However, the differences in $DoDH_{gas}$ and $DoDH_{liq}$ values of mPtA and mPt0.33MnA were larger than in Pt/gA and Pt–0.33Mn/gA (entries 3 and 4 in Table 1), which suggests that the promotion effect of Mn on the activity of Pt is strongly enhanced by using the SDP method. More specifically, the X_{H12-BT} (95.0 %) and
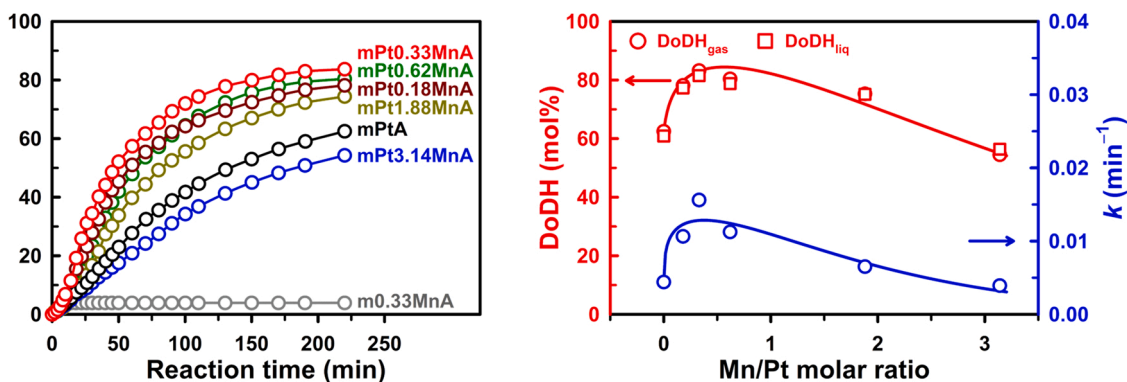

Fig. 1. Activities of the SDP-derived catalysts in the dehydrogenation of H_{12}-BT. (a) Time-dependent $DoDH_{gas}$ curves and (b) $DoDH_{gas}$, $DoDH_{liq}$, and k plotted against the Mn/Pt molar ratio. Reaction conditions: 1.5 g H_{12}-BT, 0.3 mol% Pt/H_{12}-BT, 250 °C, and 220 min.

Table 1

Catalytic performance of various Pt catalysts in the dehydrogenation of H_{12}-BT[a].

Entry	Catalyst	X_{H12-BT} [mol%]	S_{H6-BT} [mol%]	S_{H0-BT} [mol%]	S_{MF} [mol%]	$DoDH_{liq}$ [mol%]	$DoDH_{gas}$ [mol%]
1	Pt/gA	91.8	41.8	52.8	5.4	73.4	75.1
2	Pt–0.33Mn/gA	92.7	34.4	61.4	4.2	77.4	78.8
3	mPtA	79.9	48.4	49.2	2.4	60.9	62.5
4	mPt0.33MnA	95.0	29.6	66.8	3.5	81.5	83.3
5	0.33Mn/mPtA	78.4	39.2	58.9	1.9	63.3	63.9
6	Pt/m0.33MnA	88.7	42.2	53.5	4.3	70.6	72.0

[a] Reaction conditions: 1.5 g H_{12}-BT, 0.3 mol% Pt/H_{12}-BT, 250 °C, and 220 min

S_{H0-BT} (66.8 %) were significantly improved over mPt0.33MnA with a little more MF formation, compared to mPtA. Furthermore, 0.33Mn/ mPtA and Pt/m0.33MnA catalysts were prepared using the IWI method. The former catalyst (63.9 % $DoDH_{gas}$) showed negligible activity enhancement compared to mPtA (entry 5 in Table 1), implying that the

small amount of Mn added to mPtA by the IWI method hardly promotes the Pt activity. In contrast, Pt/m0.33MnA exhibited the higher $DoDH_{gas}$ and $DoDH_{liq}$ values by 9 % than mPtA (entry 6 in Table 1). Also, the S_{H0-BT} over Pt/m0.33MnA was less than over mPt0.33MnA, while more MF was formed over the former catalyst showing the lower X_{H12-BT}. The
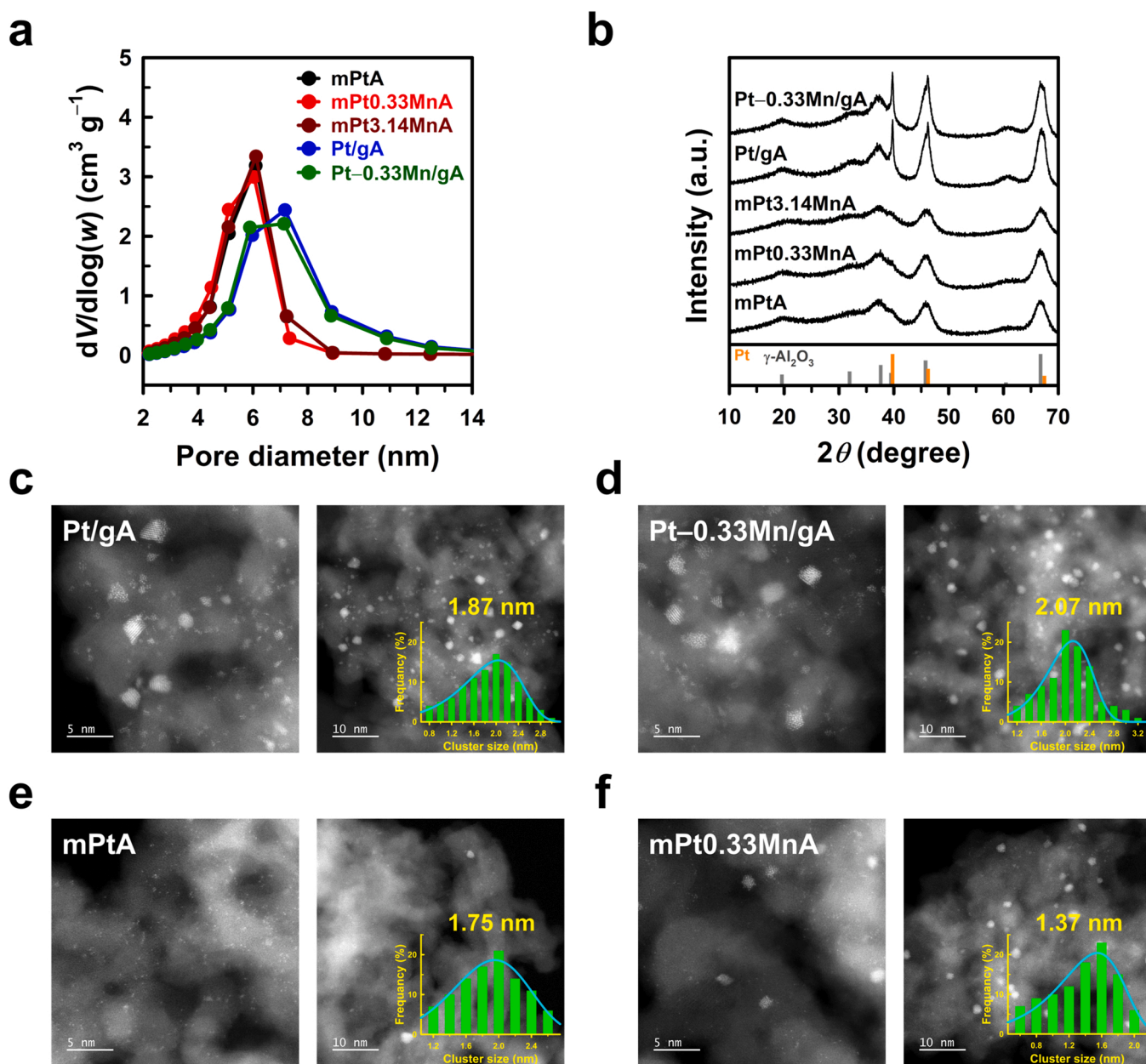

Fig. 2. (a) Pore diameter distribution curves and (b) XRD patterns of Pt/gA, Pt–0.33Mn/gA, mPtA, mPt0.33MnA, and mPt3.13MnA. (c–f) HAADF-STEM images of (c) Pt/gA, (d) Pt–0.33Mn/gA, (e) mPtA, and (f) mPt0.33MnA at different scale bars of (left) 5 and (right) 10 nm.

limited performance of these impregnated catalysts suggests that the SDP method leads to the favorable interaction between Pt and Mn species, affording the superior dehydrogenation activity of mPt0.33MnA.

The results measured by N_2 physisorption (Table S3 and Fig. S2) showed that the specific surface areas of all mPtA and mPtMnA samples (ca. 300 m^2 g^{-1}) were larger than those of Pt/gA and Pt–0.33Mn/gA (ca. 260 m^2 g^{-1}), with the slightly smaller pore volume of the former catalysts (0.52–0.57 cm^3 g^{-1}) compared to the latter (0.58 cm^3 g^{-1}). However, Fig. 2a displays the larger pore diameters of the latter catalysts (6.5 nm) than those of the former (5.0–5.3 nm). Interestingly, all textural properties of mPtMnA catalysts were little changed although the Mn/Pt molar ratio increased from 0.33–3.14. Their XRD patterns were also similar while the diffraction peaks of γ-Al_2O_3 (PDF #29–0063) were only detected (Fig. 2b), meaning the formation of small Pt species in all mPtMnA catalysts (Fig. S3). In contrast, the peak of metallic Pt at 2θ of 39.8° is much intense for Pt/gA and Pt–0.33Mn/gA.

To confirm the large difference in the XRD peak of Pt species, HAADF-STEM images were taken at two magnifications with scale bars of 5 and 10 nm for precise comparison. In the image of Pt/gA (Fig. 2c), three Pt species (SAs, NCs, and NPs) were visible although the actual Pt loading was measured to be 0.85 wt% by the ICP-OES analysis. Particularly, the presence of Pt NPs was consistent with the sharp reflection of metallic Pt in the XRD pattern of Pt/gA. The Pt species in the image of Pt–0.33Mn/gA appeared similar but were a little more aggregated (Fig. 2d). In contrast, the mPtA mainly showed Pt SAs and NCs although a few NPs were visible (Fig. 2e), which is nearly similar to the finding in our previous work [9]. Although the mPt0.33MnA looked similar to mPtA, the image with the scale bar of 10 nm indicates the increasing population of Pt NCs (ca. 1.37 nm) (Fig. 2f). From the elemental mapping images of mPt0.33MnA and mPt3.14MnA, Mn species is believed to be well distributed on Al_2O_3 (Fig. S4). Therefore, as the Mn/Pt molar ratio increased, the contact of Pt with Mn would be more probable in mPtMnA catalysts. This implies that the interaction between Pt and Mn species becomes stronger at higher Mn/Pt molar ratios.

The previous study revealed that the low dehydrogenation activity of mPtA was attributed to a large fraction of Pt SAs [9]. Therefore, the

outperformed activity of mPt0.33MnA can be explained by the formation of Pt NPs. Yet, the electronic interaction of Pt with Mn cannot be ruled out. The core level of Mn 2p was analyzed by XPS analysis but it was difficult to detect because of very low Mn contents, except mPt3.14MnA showing the presence of Mn^{3+} and Mn^{4+} in the XPS Mn 2p spectrum (Fig. S5), which is consistent with the report of Anić et al. about the promoting effect of MnO_x on Pt catalysts for hexane oxidation [23]. Therefore, the Mn species in mPtMnA catalysts would be assigned to MnO_x (a mixture of Mn_2O_3 and MnO_2). On the other hand, the Pt $4d_{3/2}$ binding energy at maximum was almost similar in the Pt 4d spectra of Pt–0.33Mn/gA and Pt/gA with the larger fraction of Pt^{2+} species for the former (Fig. 3a), meaning that Pt^{2+} species is a little formed by Pt–MnO_x interaction. In the case of mPtA, the Pt $4d_{3/2}$ binding energy measured at maximum is 315.1 eV because of Pt SAs in large populations. As more Mn was added to mPtA, the binding energy was shifted to 315.3 eV (mPt0.33MnA) and 315.4 eV (mPt3.14MnA) while the fraction of Pt^{2+} increases to 38.2 % and 51.4 % for the former and latter, respectively. These results reveal the enhanced Pt–MnO_x interaction in mPtMnA catalysts, when compared to the changes between Pt/gA and Pt–0.33Mn/gA.

The above finding was supported by H_2-TPR results (Fig. 3b). The peak of H_2 consumption was slightly shifted from 299 °C for Pt/gA to 305 °C for Pt–0.33Mn/gA, where H_2 consumption at lower temperatures corresponds to the reduction of Pt–O–Pt species [24]. In the case of mPtMnA catalysts, it increased from 303 °C (mPtA) to 312 °C (mPt0.33MnA) and 333 °C (mPt3.14MnA). Also, the shoulder peak at 355 °C (shaded in green) was observed in H_2-TPR profiles of all mPtMnA samples, where the area percentage of the corresponding peak increased from 5.3 % to 31.3 % with increasing Mn/Pt ratio (Fig. S6). Therefore, this peak can be assigned to the partially positively charged Pt species derived from the addition of Mn, which agrees with the enhanced Pt–MnO_x interaction examined from the XPS Pt 4d spectra. It is worth noting here that the electron density of Pt species in mPt3.14MnA is too much lessened, which partly explains the significantly lower dehydrogenation activity of this catalyst.

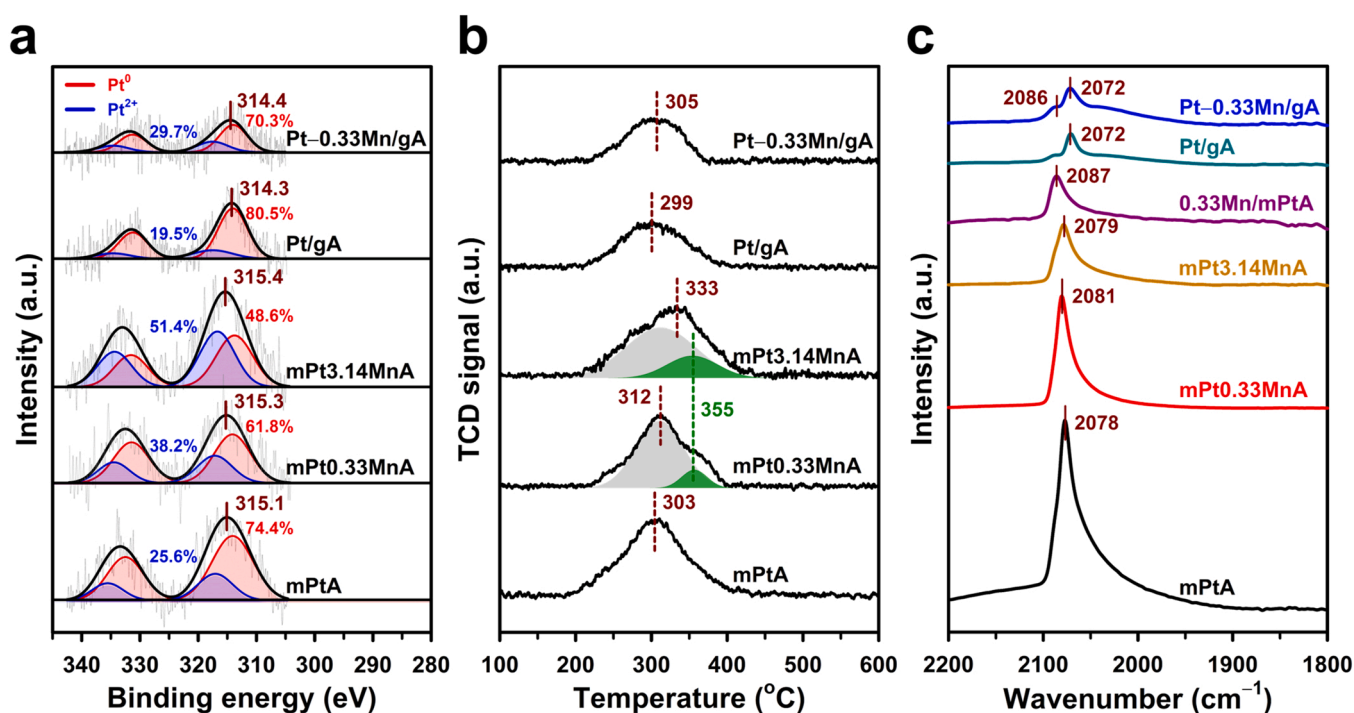Furthermore, CO-DRIFT spectra were collected to confirm the size

Fig. 3. (a) XPS Pt 4d spectra, (b) H_2-TPR profiles, and (c) CO-DRIFT spectra of Pt/gA, Pt–0.33Mn/gA, mPtA, mPt0.33MnA, and mPt3.13MnA. The panel c includes the spectrum of 0.33Mn/mPtA.

and state of Pt species. The bindings of CO with Pt atoms are classified into linear (2000–2120 cm^{-1}) and bridged types (1700–1900 cm^{-1}) [25–28], where linear binding is divided into that for Pt SAs (~2120 cm^{-1}) and Pt NCs/NPs (2060–2090 cm^{-1}). Also, the absorption bands associated with Pt NCs are detected in 2080–2090 cm^{-1} and 2060–2080 cm^{-1} assigned to partially oxidized Pt (Pt$^{\delta+}$ with δ lower than 2) and metallic Pt (Pt^0), respectively [29,30]. In the CO-DRIFT spectra of Pt/gA and Pt–0.33Mn/gA, the CO absorption peak was relatively low at 2072 cm^{-1} (Fig. 3c), indicating the formation of Pt NPs. However, a shoulder peak at 2086 cm^{-1} was larger for Pt–0.33Mn/gA than for Pt/gA, indicating the increased proportion of positively charged Pt that is caused by the Pt–MnO$_x$ interaction in Pt–0.33Mn/gA. When the CO-DRIFT spectra of mPtA and mPt0.33MnA were compared, the CO absorption band at 2120 cm^{-1}, corresponding to Pt SAs, disappeared and the peak representing Pt$^{\delta+}$ NCs was shifted from 2078 to 2081 cm^{-1} along with the reduced peak intensity. This suggests that Pt atoms are aggregated into Pt NCs and the positively charged Pt is formed by the Pt–MnO$_x$ interaction that is also capable of blocking some Pt atoms. The stronger aggregation and blocking of Pt by MnO$_x$ were identified by the much reduced peak intensity and shift to 2079 cm^{-1} for mPt3.14MnA. The CO-DRIFT spectrum of 0.33Mn/mPtA was also much reduced along with the peak centered at 2087 cm^{-1}, indicating that MnO$_x$ significantly interacts with and blocks Pt SAs of mPtA. In summary, the superior activity of mPt0.33MnA is attributed to the favorable formation of Pt NCs with a little positive charge caused by interaction with MnO$_x$. which is derived by the SDP method.

3.2. Catalytic activity and properties of the mPt0.33MnA catalysts prepared by varying a ramp rate in H$_2$ reduction

After the improved dehydrogenation activity of mPt0.33MnA was examined, we aimed to enhance the nanoclustering of Pt–MnO$_x$, leading to an increase in the catalytic activity of mPt0.33MnA. Under H$_2$ atmosphere, Pt SAs aggregate into NCs and further to NPs owing to the strong Pt–H interaction at the expense of metal-support adhesion [20],

which is largely included in the Ostwald ripening process. In this work, we adjusted the ramp rate of H$_2$ reduction, unlike the previous experiments in which temperature and H$_2$ pressure were controlled with the fixed ramp of 5 °C min^{-1}. Because the ramp rate used in the former part of work was 5 °C min^{-1}, two ramp rates of 2 and 10 °C min^{-1} were more employed, where the final reduction condition was identically set at 500 °C and 3 h.

The four catalysts (mPtA, mPt0.33MnA, Pt/gA, and Pt–0.33Mn/gA) were chosen to observe differences in reductive clustering/aggregation of Pt and/or Pt–MnO$_x$. For catalyst notation, the label (r2, r5, and r10 corresponding to the ramp rate of 2, 5, and 10 °C min^{-1}, respectively) is followed after catalyst name. As the ramp rate increased, the DoDH$_{gas}$ and k values estimated over Pt/gA were significantly lowered, while those over Pt–0.33Mn/gA were maintained at the levels of 79 % for DoDH$_{gas}$ and 0.023 min^{-1} for k (Fig. 4a). The similar trends were observed in $X_{H12\text{-}BT}$, $S_{H0\text{-}BT}$, S_{MF}, and DoDH$_{liq}$ values estimated over Pt/gA and Pt–0.33Mn/gA (Fig. 4c and Table S4). The decrease in dehydrogenation performance of Pt/gA is attributed to Pt sintering into NPs, which was confirmed by the slightly sharper peak of Pt(111) at 2θ of 39.8° with increasing the ramp rate (Fig. S7). However, the Pt sintering observed in the HAADF-STEM image of Pt–0.33Mn/gA (Fig. 2d) was not in accordance with the change in the activity of Pt–0.33Mn/gA with the increasing ramp rate. This suggests that the Pt–MnO$_x$ interaction compensates for the activity loss and hence contributes to the stable activity of Pt–0.33Mn/gA.

In contrast, the activities of mPtA and mPt0.33MnA increased with the ramp rate. Particularly, the improvement in DoDH$_{gas}$ and k values was more pronounced for mPt0.33MnA than for mPtA (Fig. 4b). From the analysis of liquid products, the calculated $X_{H12\text{-}BT}$ (77.3–98.6 %), $S_{H0\text{-}BT}$ (49.1–76.7 %), S_{MF} (1.9–7.1 %), and DoDH$_{liq}$ (58.6–91.8 %) over mPt0.33MnA were found to be much increased at faster ramps compared to those over mPtA (Fig. 4d and Table S4). Consequently, the mPt0.33MnA_r10 exhibited the highest values of DoDH$_{liq}$ (92 %) and DoDH$_{gas}$ (94 %) among all of the prepared catalysts in this work and furthermore, it was more active than state-of-the-art catalysts
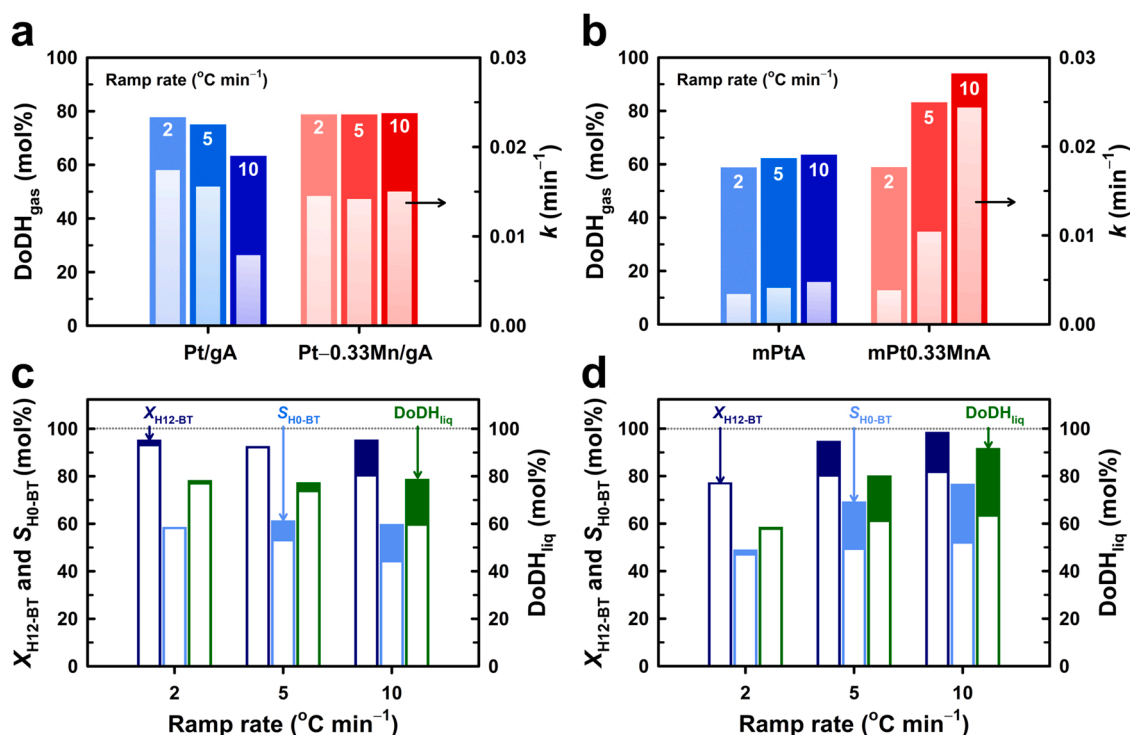

Fig. 4. Catalytic performance of (a,c) Pt/gA and Pt–0.33Mn/gA; (b,d) mPtA and mPt0.33MnA prepared by using the ramp rate of 2, 5, and 10 °C min^{-1} in H$_2$ reduction. (a,b) DoDH$_{gas}$ (colored bars) and k calculated from Fig. S8 (white bars). (c,d) $X_{H12\text{-}BT}$, $S_{H0\text{-}BT}$, and DoDH$_{liq}$ of Pt–0.33Mn/gA and mPt0.33MnA (colored bars) compared to Pt/gA and mPtA (white bars). Reaction conditions: 1.5 g H$_{12}$-BT, 0.3 mol% Pt/H$_{12}$-BT, 250 °C, 200 rpm, and 220 min.

(Table S4). Although the ramp rate in H_2 reduction varied for mPtA and mPt0.33MnA catalysts, their textural properties (e.g., specific surface area, pore volume, and pore size) were negligibly changed (Table S5). Also, the contents of Pt were similar at 0.83–0.85 wt% for all samples while those of Mn in the mPt0.33MnA catalysts were almost constant at 0.077 wt% (Table S5). Therefore, it is believed that tuning the ramp rate in H_2 reduction is effective for the nanoclustering of Pt–MnO_x in the mPtMnA catalysts derived by the SDP method.

To find the evidences for the nanoclustering of Pt–MnO_x, we compared the HADDF-STEM images of mPtA and mPt0.33MnA catalysts prepared by H_2 reduction at different ramp rates (Fig. 5). The images of mPtA_r2 and mPtA_r5 showed mainly Pt SAs with the small population of NCs and NPs. The Pt nanoclustering and aggregation were evident in the image of mPtA_r10, which indicates that strong Pt mobility happens at the ramp of 10 °C min^{-1} in H_2 reduction. The similar observation was seen for mPt0.33MnA catalysts: Pt SAs, which were dominant in the image of mPt0.33MnA_r2, tended to be changed into Pt NCs at the ramp of 5 and 10 °C min^{-1}, resulting in a higher population of Pt NCs in the image of mPt0.33MnA_r10. Also, the remarkable point is that the average size of Pt NCs in mPt0.33MnA_r5 and mPt0.33MnA_r10 was nearly identical at ca. 1.3 nm (Fig. S9). This implies that the growth of Pt NCs into NPs at a higher ramp rate is inhibited by the MnO_x present in mPt0.33MnA possibly because of the nanoclustering of Pt–MnO_x. Then, we tried to visualize the proximity between Pt species and MnO_x of such NCs through elemental mapping of mPt0.33MnA_r5 (Fig. S4a) and mPt0.33MnA_r10 (Fig. S10), yet it was very hard to clearly confirm it

due to the low Mn content (0.077 wt% in Table S5).

Thus, XPS analysis and CO-DRIFT experiments were conducted to examine electronic changes of Pt species by Pt–MnO_x nanoclustering. At first, XPS Pt spectra showed interesting differences in the binding energy of Pt $4d_{5/2}$ core level and the Pt^0 fraction estimated by peak deconvolution (Fig. S11). When the spectra of Pt/gA and mPtA were compared (Fig. 6a), the binding energy was negligibly changed at 314.3–314.5 eV for Pt/gA and at 315.0–315.1 eV for mPtA as the ramp rate increased from 2° to 10°C min^{-1}. The area fraction of Pt^0 was also increased from 74.1 % to 87.9 % for Pt/gA and from 69.5 % to 82.7 % for mPtA. Such results are considered to originate from the increase in the size of Pt species with the decreasing Pt–Al interaction: specifically, aggregation of Pt NPs for Pt/gA and nanoclustering of Pt SAs for mPtA. In contrast, when the XPS $4d_{5/2}$ spectra of Pt–0.33Mn/gA and mPt0.33MnA were compared with respect to the ramp rate, the binding energy was maintained at 314.5 eV for Pt–0.33Mn/gA but it was shifted from 315.1 to 315.7 eV for mPt0.33MnA. Furthermore, the area fraction of Pt^0 was more reduced in mPt0.33MnA (from 68.4 % to 45.2 %) than in Pt–0.33Mn/gA (from 71.2 % to 67.7 %). These XPS results (i.e., shift to higher binding energy and smaller Pt^0 fraction) indicate the lowered electron density of Pt in mPt0.33MnA_r10 due to the electron transfer to Mn species attributed to the nanoclustering of Pt–MnO_x.

Furthermore, CO-DRIFT experiments were carried out for a series of mPtA and mPt0.33MnA catalysts in order to elucidate the Pt–MnO_x nanoclustering. It is worth noting that all spectra were obtained after the 15-min desorption of CO in an Ar flow, because no change was observed
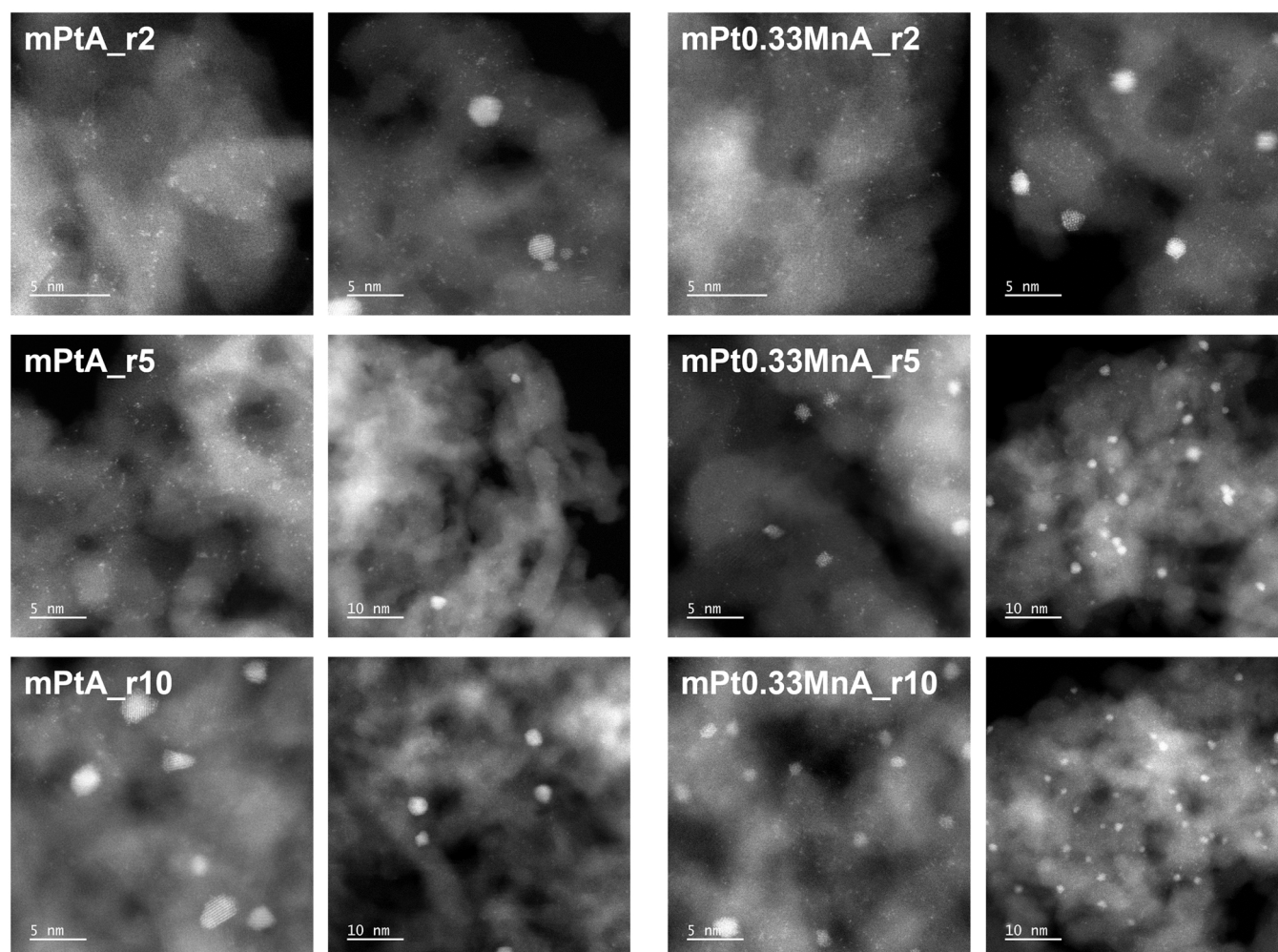

Fig. 5. HAADF-STEM images of the mPtA and mPt0.33MnA catalysts reduced with varying the ramp rate. For each catalyst, the high-magnification images are on the left and the low-magnification images are on the right.
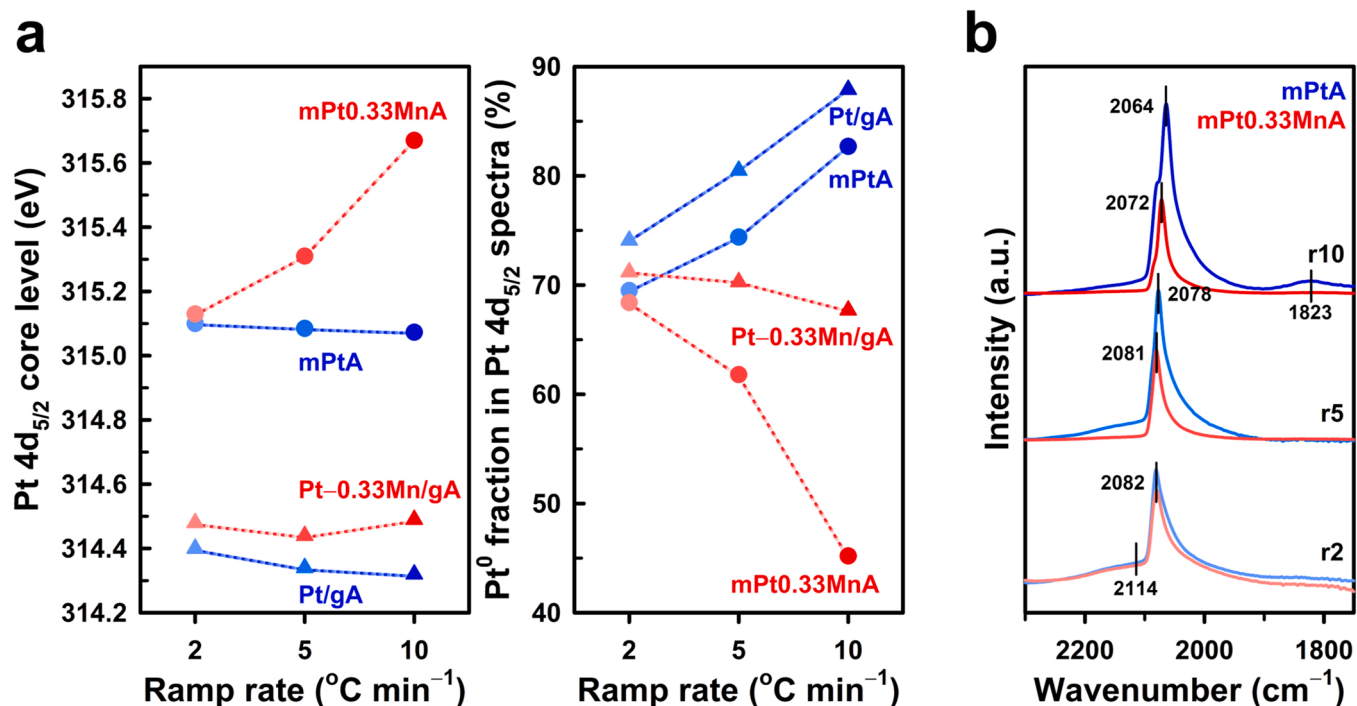
Fig. 6. (a) Binding energy and Pt[0] fraction measured from XPS Pt 4d spectra of Pt/gA, Pt–0.33Mn/gA, mPtA, and mPt0.33MnA, and (b) CO-DRIFT spectra of mPtA and mPt0.33MnA. All catalysts were prepared by varying the ramp rate in H_2 reduction at 2, 5, and 10 °C min^{-1}.

in the spectra taken at 10 and 15 min (Fig. S12). The spectra of mPtA_r2 and mPt0.33MnA_r2 were very similar (Fig. 6b), showing the peaks appeared at 2114 and 2082 cm^{-1} corresponding to Pt SAs and Pt$^{\delta+}$ NCs, respectively. However, the spectra of two catalysts reduced at the ramp of 5 °C min^{-1} were different. For mPt0.33MnA_r5, the peak at 2114 cm^{-1} disappeared and the peak at 2082 cm^{-1} was negligibly

shifted. In contrast, the former peak still remained and the latter peak moved to 2078 cm^{-1} in the spectrum of mPtA_r5, meaning the co-existence of Pt SAs, NCs, and NPs. Such differences originate from the nanoclustering of Pt atoms owing to the MnO$_x$ present in mPt0.33MnA_r5.

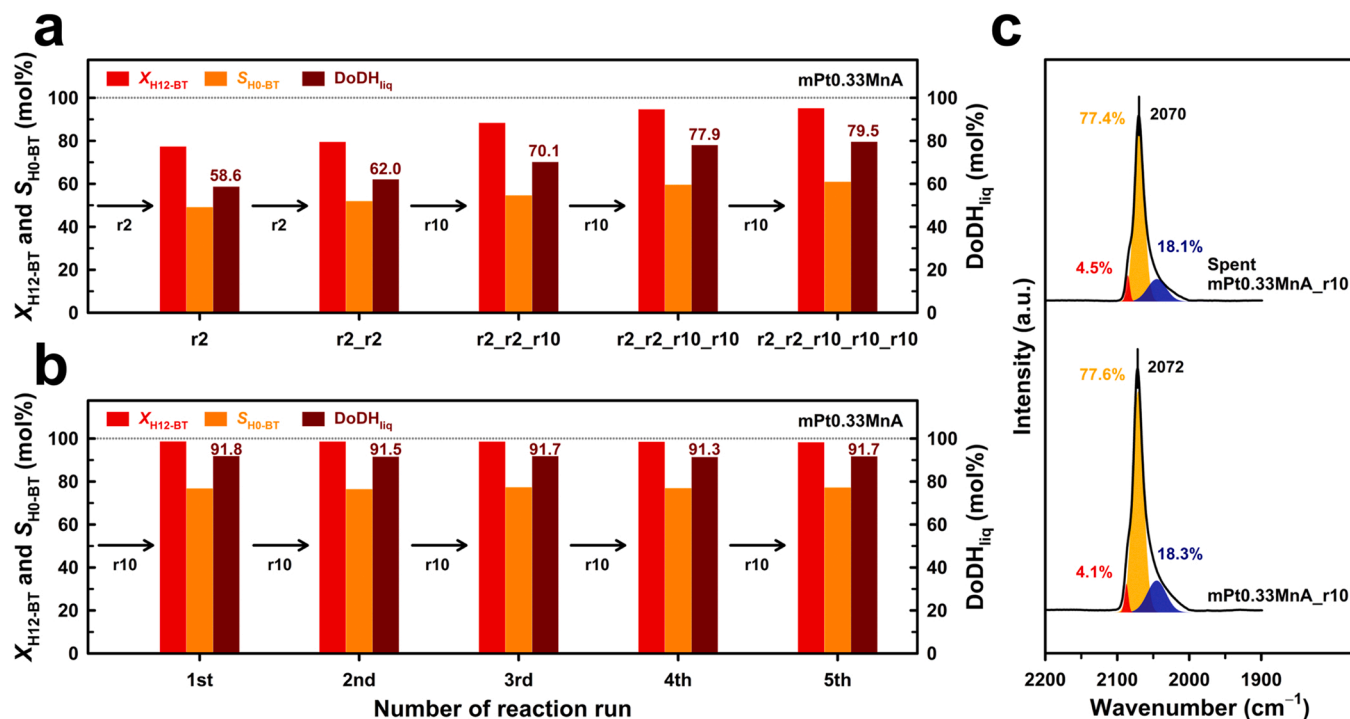This was more obvious in the samples prepared by H_2 reduction at

Fig. 7. Activities ($X_{\text{H12-BT}}$, $S_{\text{H0-BT}}$, and DoDH$_{\text{liq}}$) of mPt0.33MnA catalysts obtained (a) through sequential H_2 reduction and (b) by H_2 reduction at the ramp of 10 °C min^{-1} after the reaction. (c) CO-DRIFT spectra of fresh mPt0.33MnA_r10 and its fifth-recycled catalysts. Reaction conditions: 1.5 g H_{12}-BT, 0.3 mol% Pt/H_{12}-BT, 250 °C, 200 rpm, and 220 min.

the ramp of 10 °C min^{-1}. The mPtA_r10 showed the absorption peaks at 2114, 2072, 2064, and 1823 cm^{-1}. The peak at 2064 cm^{-1}), corresponding to the linear binding of CO to Pt NPs, was more intense than the peak from mPtA_r5, and the new peak was found at 1823 cm^{-1} for the bridged binding of CO, which is strong evidence for the growth of Pt SAs and/or NCs to NPs. This agrees with the XPS Pt 4d results of mPtA_r10. However, the mPt0.33MnA_r10 exhibited only the peak at 2072 cm^{-1} with no peak in the range 1700–2000 cm^{-1}. This confirms that the growth to Pt NPs is suppressed in mPt0.33MnA_r10, unlike mPtA_r10, possibly by the nanoclustering of Pt with MnO$_x$ leading to the lowered electron density of Pt examined by XPS analysis.

3.3. Activities of mPt0.33MnA catalysts in repeated runs

The above work revealed that the ramp rate in H$_2$ reduction could control the nanoclustering of Pt and MnO$_x$. Thus, we attempted to confirm such a finding through repeated reduction or activity runs over mPt0.33MnA obtained by H$_2$ reduction at the ramp of 2 or 10 °C min^{-1}. The fresh mPt0.33MnA_r2 showed 58.6 % DoDH$_{liq}$ and 49 % S_{H0-BT}, while the catalyst reduced again at the ramp of 2 °C min^{-1} exhibited 62.0 % DoDH$_{liq}$ and 52 % S_{H0-BT} (Fig. 7a). This means that although a few Pt NCs are formed, most of Pt SAs in the fresh mPt0.33MnA_r2 still remain even after the second H$_2$ reduction at the same ramp. Then, the ramp rate was changed to 10 °C min^{-1} for the next three runs. As a result of repeating this reduction process, the higher DoDH$_{liq}$ values of 70.1 %, 77.9 %, and 79.5 % were achieved: moreover, the S_{H0-BT} increased from 54.5 % to 59.5 % and further to 60.9 % with a very small increment in S_{MF} (2.5–3.3 %). These values were considerably higher than the DoDH$_{liq}$ of mPtA_r10 (63.1 %), which is caused by the interaction between Pt species and MnO$_x$ along with the decreasing population of Pt SAs. Also, the increasing activity in repeated runs employing the ramp of

10 °C min^{-1} indicate the contribution of Pt–MnO$_x$ NCs to the superior performance of mPt0.33MnA_r10.

On the other hand, the remarkable stability of mPt0.33MnA_r10 was demonstrated in five repeated experiments of dehydrogenation reaction and H$_2$ reduction (10 °C min^{-1} ramp), affording the stable DoDH$_{liq}$ of 91 % (Fig. 7b). Moreover, the S_{H0-BT} and S_{MF} values remained at 77 $\pm$ 1 % and 7 $\pm$ 0.1 % in all experimental results, respectively. This result is a convincing evidence for the robustness of Pt–MnO$_x$ NCs. If a fast ramp in H$_2$ reduction makes Pt SAs to aggregate into NPs, then the activity of mPt0.33MnA_r10 would continuously decrease in repeated runs. Since this assumption is not compatible with the observation, the Pt–MnO$_x$ NCs formed at the first step of H$_2$ reduction would be robust with minimal changes in the structural and electronic characters of Pt species. This presumption was verified by comparing the CO-DRIFT spectrum of mPt0.33MnA_r10 with that of its fifth-recycled catalyst. As shown in Fig. 7c, the spectra of the two samples were almost indistinguishable with the very small shift of 2 cm^{-1}. The calculated area fractions of three peaks obtained after deconvolution were hardly changed at ca. 4.3 % (Pt$^{\delta+}$ NCs), 77.5 % (Pt^0 NCs), and 18.2 % (NPs). This means that the Pt–MnO$_x$ NCs are maintained even though the dehydrogenation experiment and catalyst activation by H$_2$ reduction were repeated five times, which is consistent to the stable activity of mPt0.33MnA_r10. Moreover, the HAADF-STEM image of mPt0.33MnA_r10 obtained after 5 cycles did not show aggregated Pt NPs (Fig. S13).

3.4. Discussion on structural features of mPtMnA catalysts

In the nanostructure of gA, bridging Al atoms to stabilize stacking faults are closely related to the generation of penta-coordinated Al [31]. In case of mesoporous Al$_2$O$_3$ (mA) that is the major component of mPtMnA catalysts, boehmite (AlO(OH))-like defects are created,
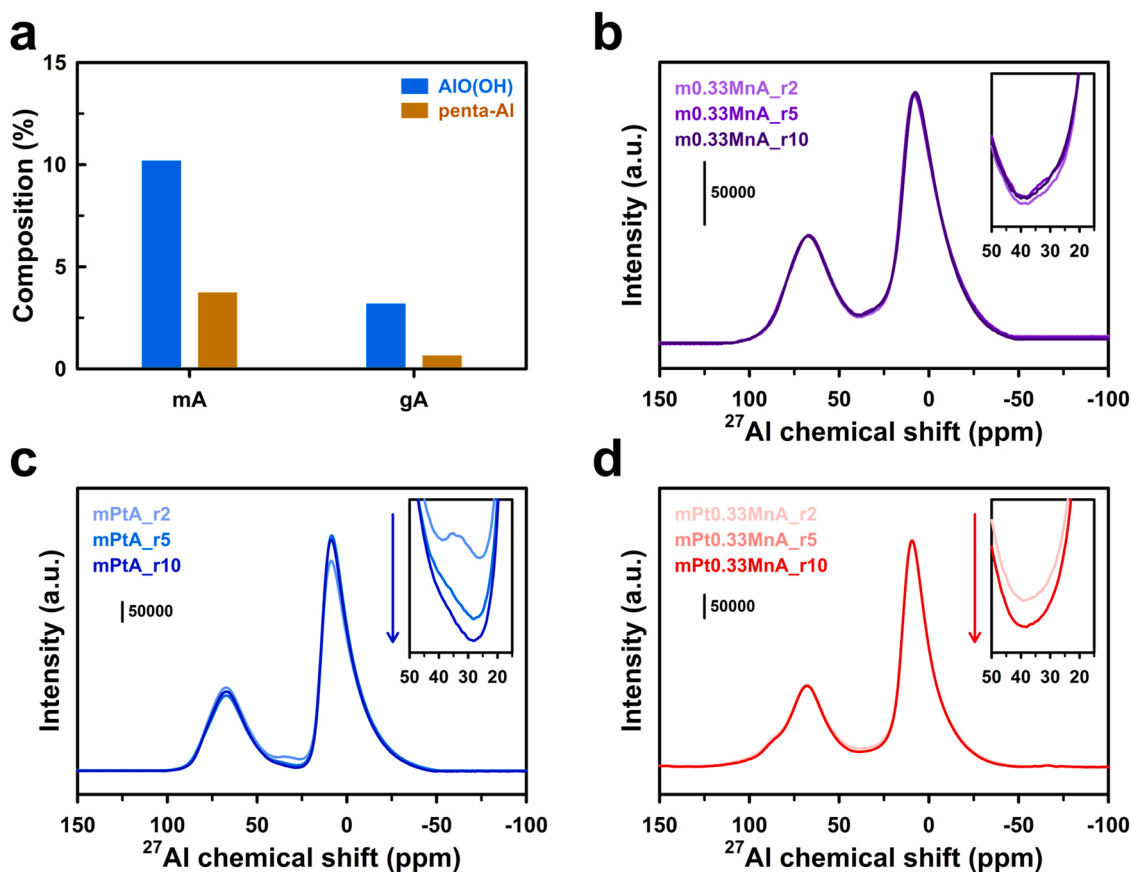

Fig. 8. (a) Fractions of AlO(OH) and Al^v sites in mA and gA measured by XPS and ^{27}Al MAS NMR results, respectively. (b–d) ^{27}Al MAS NMR spectra of (b) m0.33MnA, (c) mPtA, and (d) mPt0.33MnA prepared by H$_2$ reduction at different ramp rates of 2, 5, and 10 °C min^{-1}.

because of a solvent-poor condition, and gradually disappear at high calcination temperatures [32].

Thus, the mA and gA supports were characterized by XPS and ^{27}Al MAS NMR analyses (Fig. 8a). In the region of XPS Al 2p core level showing two deconvoluted peaks (Fig. S14a), the peak at a higher binding energy of 75.2 eV was associated with boehmite-like defects because their amount decreased as thermal treatment became severe (not shown here for brevity). When the spectrum of mA was compared with that of gA, the former support contained a larger amount of such defects (10.2 %) than the latter (3.2 %). In ^{27}Al MAS NMR spectra (Fig. S14b), three characteristic peaks are generally detected around 0, 30, and 70 ppm assigned to octahedral, penta-coordinated (Al^v), and tetrahedral Al sites, respectively. The NMR spectra revealed that the mA contained a higher fraction of penta-coordinated Al sites (3.75 %) than the gA (0.66 %). Therefore, the structural defects of mA, caused by the solvent-deficient environment, are linked to its Al^v sites, as already identified for the gA. Moreover, the mA samples reduced at the ramp of 2, 5, and 10 °C min^{-1} did not show a difference in the peak of Al^v species around 30 ppm (Fig. S15), implying that structural defect-healing does not occur in Al$_2$O$_3$ alone under the employed H$_2$ reduction conditions.

To understand the mobility of Mn species in mPt0.33MnA, a mesoporous 3 wt% Mn–Al$_2$O$_3$ (m3MnA) was prepared by the SDP method, followed by calcination at 600 °C (named C600) and H$_2$ reduction at 500 °C (named R500). The XPS Mn 2p spectra of two samples showed that the area percentages of Mn^{3+} and Mn^{4+} were not changed before and after H$_2$ reduction (Fig. S16a), Also, there was no change in the XRD peaks of the calcined and reduced m3MnA forms (Fig. S16b). This suggests that the Mn species as MnO$_x$ has very little mobility on the mA support under the employed H$_2$ reduction conditions, possibly due to the oxophilic character of Mn species. Furthermore, when the m0.33MnA was reduced at different ramp rates, the ^{27}Al MAS NMR spectra were nearly identical (Fig. 8b). This means that the Mn oxides are hardly mobile in H$_2$ reduction due to homogeneous mixing with Al$_2$O$_3$, which was also examined in mPt0.33MnA_r5 and mPt0.33MnA_r10 by elemental mapping.

The Al^v sites in alumina is coordinatively unsaturated and form Pt SAs with a Pt–O–Al bond when Pt species are added, thereby improving Pt dispersion [3]. Thus, Pt SAs were more formed in mPtA than in Pt/gA. When combined with the suppressed Ostwald ripening of metal particles due to the lack of solvent during grinding in the SDP process [9,22,33, 34], Pt SAs on mPtA are believed to be anchored onto the defect sites in the proximity of Al^v sites. Thereafter, the Pt–O–Al bonds are dissociated under reductive atmosphere and Pt atoms are then susceptible to surface diffusion on the surface of mA and Pt aggregation [20], because the reduction temperature (500 °C) is higher than Pt's Hüttig temperature (335 °C) that is a temperature necessary for surface recrystallization of metal or metal oxide. Therefore, the results shown in Figs. 5 and 6 manifest that the mobility of Pt atoms depends on the ramp rate in H$_2$ reduction. Particularly, it was found that the peak of Al^v sites was significantly lessened as the ramp rate in H$_2$ reduction increased (Fig. 8c). This suggests that Pt atoms are surface-diffused onto another defect sites close to Al^v sites and then gathered into Pt NCs and NPs at the ramp rate of 5 and 10 °C min^{-1}, respectively, which was evidenced by HAADF-STEM images, XPS Pt 4d spectra, and CO-DRIFT spectra of the mPtA catalysts.

Finally, the ^{27}Al MAS NMR spectra of mPt0.33MnA catalysts were compared with those of mPtA catalysts. The most remarkable difference was that the peak of Al^v species around 30 ppm was reduced between mPtMnA_r2 and mPtMnA_r5 and was changed no more for mPtMnA_r10 (Fig. 8d). As discussed in mPtA catalysts, the Pt–O–Al bonds in mPt0.33MnA are dissociated and Pt NCs are formed near defect sites close to Al^v sites by increasing the ramp rate from 2° to 5°C min^{-1}. However, the further increase to 10 °C min^{-1} did not make any change in the Al species of mPt0.33MnA, which is a big difference between mPtA_r10 and mPt0.33MnA_r10. In addition, the peak of Al^v species was much higher for all mPtMnA catalysts than for all mPtA ones. This

suggests that in H$_2$ reduction, mobile Pt SAs are preferentially diffused to Mn oxide species rather than to Al species, hence generating highly dispersed Pt–MnO$_x$ NCs in mPt0.33MnA_r10 showing the outstanding dehydrogenation activity.

4. Conclusions

This study started investigating the effect of Mn/Pt molar ratio on the activity and properties of mPtMnA catalysts prepared by the SDP method. The mPt0.33MnA exhibited the better dehydrogenation performance than other mPtMnA catalysts and IWI-derived Pt−Mn catalysts, resulting from the favorable formation of Pt NCs with a little positive charge caused by interaction with MnO$_x$. Moreover, the higher ramp rate in H$_2$ reduction of mPt0.33MnA led to activity improvement, which was quite different from the Pt− 0.33Mn/gA. The formed NCs in the mPt0.33MnA_r10 were demonstrated to be robust in repeated dehydrogenation runs. The SDP process working under solvent-poor conditions generated boehmite-like defect sites in the proximity of Al^v sites of the mA compared to the gA, contributing to pronounced formation of Pt SAs with Pt–O–Al bonds in both mPtA and mPtMnA. While these bonds are dissociated at a higher ramp rate, Pt SAs are expected to aggregate into NCs and NPs under reductive atmosphere. This was clearly examined in mPtA but not in mPtMnA catalysts. This difference possibly resulted from homogeneous distribution of oxophilic Mn oxides on the support surface. In other words, Pt atoms are surface-diffused preferentially to Mn oxides, yielding highly dispersed Pt–MnO$_x$ NCs. This explains the outperformed dehydrogenation activity of mPtMnA_r10. Consequently, the overall catalyst preparation based on the SDP method is so simple and unique in the formation of Pt–MnO$_x$ NCs that it is worth being applied for a variety of highly dispersed NCs composed of metal(s) and metal oxide(s).

CRediT authorship contribution statement

Yeongin Jo: Investigation, Formal analysis, Data curation, Writing - original draft. **Donghyeon Kim**: Investigation, Formal analysis, Data curation, Writing - original draft. **Tae Wan Kim:** Investigation, Formal analysis, Data curation. **Doohoo Yoon**: Investigation, Formal analysis, Data curation. **Young-Woong Suh:** Conceptualization, Supervision, Funding acquisition, Writing - review & editing.

Declaration of Competing Interest

The authors declare no competing financial interests. The authors declare that they have no known competing financial interests or personal relationships that could have appeared to influence the work reported in this paper.

Data availability

Data will be made available on request.

Acknowledgements

Appendix A. Supporting information

Supplementary data associated with this article can be found in the online version at doi:10.1016/j.apcatb.2023.122848.

References

[1] J.J.H.B. Sattler, J. Ruiz-Martinez, E. Santillan-Jimenez, B.M. Weckhuysen, Catalytic dehydrogenation of light alkanes on metals and metal oxides, Chem. Rev. 114 (2014) 10613–10653.

[2] Y. Dai, X. Gao, Q. Wang, X. Wan, C. Zhou, Y. Yang, Recent progress in heterogeneous metal and metal oxide catalysts for direct dehydrogenation of ethane and propane, Chem. Soc. Rev. 50 (2021) 5590–5630.

[3] J.H. Kwak, J. Hu, D. Mei, C.-W. Yi, D.H. Kim, C.H.F. Peden, L.F. Allard, J. Szanyi, Coordinatively unsaturated Al^{3+} centers as binding sites for active catalyst phases of platinum on γ-Al_2O_3, Science 325 (2009) 1670–1673.

[4] W. Zhang, H. Wang, J. Jiang, Z. Sui, Y. Zhu, D. Chen, X. Zhou, Size dependence of Pt catalysts for propane dehydrogenation: from atomically dispersed to nanoparticles, ACS Catal. 10 (2020) 12932–12942.

[5] W. Chen, J. Ji, X. Feng, X. Duan, G. Qian, P. Li, X. Zhou, D. Chen, W. Yuan, Mechanistic insight into size-dependent activity and durability in Pt/CNT catalyzed hydrolytic dehydrogenation of ammonia borane, J. Am. Chem. Soc. 136 (2014) 16736–16739.

[6] K. Kon, S.M.A. Hakim Siddiki, K.-i Shimizu, Size- and support-dependent Pt nanocluster catalysis for oxidant-free dehydrogenation of alcohols, J. Catal. 304 (2013) 63–71.

[7] Y.-X. Tuo, L.-J. Shi, H.-Y. Cheng, Y.-A. Zhu, M.-L. Yang, J. Xu, Y.-F. Han, P. Li, W.-K. Yuan, Insight into the support effect on the particle size effect of Pt/C catalysts in dehydrogenation, J. Catal. 360 (2018) 175–186.

[8] W. Zhao, C. Chizallet, P. Sautet, P. Raybaud, Dehydrogenation mechanisms of methyl-cyclohexane on γ-Al_2O_3 supported Pt_{13}: Impact of cluster ductility, J. Catal. 370 (2019) 118–129.

[9] J. Oh, Y. Jo, T.W. Kim, H.B. Bathula, S. Yang, J.H. Baik, Y.-W. Suh, Highly efficient and robust Pt ensembles on mesoporous alumina for reversible H_2 charge and release of commercial benzyltoluene molecules, Appl. Catal. B Environ. 305 (2022) 121061.

[10] T.W. Kim, Y. Jo, K. Jeong, H. Yook, J.W. Han, J.H. Jang, G.B. Han, J.H. Park, Y.-W. Suh, Tuning the isomer composition is a key to overcome the performance limits of commercial benzyltoluene as liquid organic hydrogen carrier, J. Energy Storage 60 (2023) 106676.

[11] M. Peng, C. Dong, R. Gao, D. Xiao, H. Liu, D. Ma, Fully exposed cluster catalyst (FECC): toward rich surface sites and full atom utilization efficiency, ACS Cent. Sci. 7 (2021) 262–273.

[12] Y. Jo, J. Oh, D. Kim, J.H. Park, J.H. Baik, Y.-W. Suh, Recent progress in dehydrogenation catalysts for heterocyclic and homocyclic liquid organic hydrogen carriers, Korean J. Chem. Eng. 39 (2022) 20–37.

[13] X. Fan, D. Liu, X. Sun, X. Yu, D. Li, Y. Yang, H. Liu, J. Diao, Z. Xie, L. Kong, X. Xiao, Z. Zhao, Mn-doping induced changes in Pt dispersion and Pt_xMn_y alloying extent on Pt/Mn-DMSN catalyst with enhanced propane dehydrogenation stability, J. Catal. 389 (2020) 450–460.

[14] A. Nakano, S. Manabe, T. Higo, H. Seki, S. Nagatake, T. Yabe, S. Ogo, T. Nagatsuka, Y. Sugiura, H. Iki, Y. Sekine, Effects of Mn addition on dehydrogenation of methylcyclohexane over Pt/Al_2O_3 catalyst, Appl. Catal. A Gen. 543 (2017) 75–81.

[15] H. Yan, S. Yao, J. Wang, S. Zhao, Y. Sun, M. Liu, X. Zhou, G. Zhang, X. Jin, X. Feng, Y. Liu, X. Chen, D. Chen, C. Yang, Engineering Pt-Mn_2O_3 interface to boost selective oxidation of ethylene glycol to glycolic acid, Appl. Catal. B Environ. 284 (2021) 119803.

[16] Z. Wu, B.C. Bukowski, Z. Li, C. Milligan, L. Zhou, T. Ma, Y. Wu, Y. Ren, F. H. Ribeiro, W.N. Delgass, J. Greeley, G. Zhang, J.T. Miller, Changes in catalytic and adsorptive properties of 2 nm Pt_3Mn nanoparticles by subsurface atoms, J. Am. Chem. Soc. 140 (2018) 14870–14877.

[17] L. Rochlitz, Q. Pessemesse, J.W.A. Fischer, D. Klose, A.H. Clark, M. Plodinec, G. Jeschke, P.-A. Payard, C. Copéret, A robust and efficient propane dehydrogenation catalyst from unexpectedly segregated Pt_2Mn nanoparticles, J. Am. Chem. Soc. 144 (2022) 13384–13393.

[18] D. Yan, J. Chen, H. Jia, Temperature-induced structure reconstruction to prepare a thermally stable single-atom platinum catalyst, Angew. Chem. Int. Ed. 59 (2020) 13562–13567.

[19] X. Yao, Y. Wei, Z. Wang, L. Gan, Revealing the role of surface composition on the particle mobility and coalescence of carbon-supported Pt alloy fuel cell catalysts by in situ heating (S)TEM, ACS Catal. 10 (2020) 7381–7388.

[20] C. Dessal, A. Sangnier, C. Chizallet, C. Dujardin, F. Morfin, J.-L. Rousset, M. Aouine, M. Bugnet, P. Afanasiev, L. Piccolo, Atmosphere-dependent stability and mobility of catalytic Pt single atoms and clusters on γ-Al_2O_3, Nanoscale 11 (2019) 6897–6904.

[21] T.W. Kim, M. Kim, S.K. Kim, Y.N. Choi, M. Jung, H. Oh, Y.-W. Suh, Remarkably fast low-temperature hydrogen storage into aromatic benzyltoluenes over MgO-supported Ru nanoparticles with homolytic and heterolytic H_2 adsorption, Appl. Catal. B Environ. 286 (2021), 119889.

[22] Y. Jo, T.W. Kim, J. Oh, D. Kim, Y.-W. Suh, Mesoporous sulfur-decorated Pt–Al_2O_3 for dehydrogenation of perhydro benzyltoluenes: activity-favorable adsorption of reaction species onto electron-deficient Pt atoms, J. Catal. 413 (2022) 127–137.

[23] M. Anić, N. Radić, B. Grbić, V. Dondur, L. Damjanović, D. Stoychev, P. Stefanov, Catalytic activity of Pt catalysts promoted by MnO_x for n-hexane oxidation, Appl. Catal. B Environ. 107 (2011) 327–332.

[24] J. Lee, E.J. Jang, D.G. Oh, J. Szanyi, J.H. Kwak, Morphology and size of Pt on Al_2O_3: The role of specific metal-support interactions between Pt and Al_2O_3, J. Catal. 385 (2020) 204–212.

[25] C. Wang, X.-K. Gu, H. Yan, Y. Lin, J. Li, D. Liu, W.-X. Li, J. Lu, Water-mediated Mars–Van Krevelen mechanism for CO oxidation on ceria-supported single-atom Pt_1 catalyst, ACS Catal. 7 (2017) 887–891.

[26] B. Han, Y. Guo, Y. Huang, W. Xi, J. Xu, J. Luo, H. Qi, Y. Ren, X. Liu, B. Qiao, T. Zhang, Strong metal–support interactions between Pt single atoms and TiO_2, Angew. Chem. Int. Ed. 59 (2020) 11824–11829.

[27] X. Zhang, G. Cui, H. Feng, L. Chen, H. Wang, B. Wang, X. Zhang, L. Zheng, S. Hong, M. Wei, Platinum–copper single atom alloy catalysts with high performance towards glycerol hydrogenolysis, Nat. Commun. 10 (2019) 5812.

[28] K. Ding, A. Gulec, A.M. Johnson, N.M. Schweitzer, G.D. Stucky, L.D. Marks, P. C. Stair, Identification of active sites in CO oxidation and water-gas shift over supported Pt catalysts, Science 350 (2015) 189–192.

[29] B. Qiao, A. Wang, X. Yang, L.F. Allard, Z. Jiang, Y. Cui, J. Liu, J. Li, T. Zhang, Single-atom catalysis of CO oxidation using Pt_1/FeO_x, Nat. Chem. 3 (2011) 634–641.

[30] C. Dessal, T. Len, F. Morfin, J.-L. Rousset, M. Aouine, P. Afanasiev, L. Piccolo, Dynamics of single Pt atoms on alumina during CO oxidation monitored by *Operando* X-ray and infrared spectroscopies, ACS Catal. 9 (2019) 5752–5759.

[31] G. Paglia, E.S. Božin, S.J.L. Billinge, Fine-scale nanostructure in γ-Al_2O_3, Chem. Mater. 18 (2006) 3242–3248.

[32] S.J. Smith, S. Amin, B.F. Woodfield, J. Boerio-Goates, B.J. Campbell, Phase progression of γ-Al_2O_3 nanoparticles synthesized in a solvent-deficient environment, Inorg. Chem. 52 (2013) 4411–4423.

[33] H.B. Bathula, J. Oh, Y. Jo, Y.-W. Suh, Dehydrogenation of 2-[(n-methylcyclohexyl) methyl]piperidine over mesoporous Pd-Al_2O_3 catalysts prepared by solvent deficient precipitation: influence of calcination conditions, Catalysts 9 (2019) 719.

[34] J. Oh, H.B. Bathula, J.H. Park, Y.-W. Suh, A sustainable mesoporous palladium-alumina catalyst for efficient hydrogen release from N-heterocyclic liquid organic hydrogen carriers, Commun. Chem. 2 (2019) 68.